

GA-A23078

**TIME-DEPENDENT TRANSPORT SIMULATIONS
OF JET H-MODE PLASMAS**

by
J.E. KINSEY

MARCH 1999

DISCLAIMER

This report was prepared as an account of work sponsored by an agency of the United States Government. Neither the United States Government nor any agency thereof, nor any of their employees, makes any warranty, express or implied, or assumes any legal liability or responsibility for the accuracy, completeness, or usefulness of any information, apparatus, product, or process disclosed, or represents that its use would not infringe privately owned rights. Reference herein to any specific commercial product, process, or service by trade name, trademark, manufacturer, or otherwise, does not necessarily constitute or imply its endorsement, recommendation, or favoring by the United States Government or any agency thereof. The views and opinions of authors expressed herein do not necessarily state or reflect those of the United States Government or any agency thereof.

TIME-DEPENDENT TRANSPORT SIMULATIONS OF JET H-MODE PLASMAS

by
J.E. KINSEY*

This is a preprint of a paper presented at the 17th International Atomic Energy Agency Fusion Energy Conference, October 19-24, 1998, Yokohama, Japan and to be published in *Nucl. Fusion*.

*Oak Ridge Associated Universities, Oak Ridge, Tennessee.

**Work supported by
the U.S. Department of Energy under
Grant No. DE-FG03-95ER54309**

**GA PROJECT 03726
MARCH 1999**

Abstract

A drift wave based transport model is used to self-consistently predict the time evolution of temperature and density profiles in JET H-mode tokamak discharges. It is found that the same theoretically derived gyroBohm transport model previously used to simulate systematic scans of L-mode discharges is equally successful in modeling JET ELMy H-mode plasmas, implying that core transport is not intrinsically different from L-mode confinement. The only difference between the L-mode and H-mode simulations results from the boundary conditions (i.e., density and temperature pedestals), which are taken from experimental data in both cases. Here, standardized experimental data from 16 JET H-mode discharges in the ITER Profile Database is used including dimensionless parameter scans in relative gyroradius ρ_* , collisionality ν , and plasma β . Imperfections in dimensionless similarity for three pairs of scans in relative gyro-radius cause a purely gyro-Bohm transport model to exhibit worse than gyroBohm confinement. For the β scan, the model indicates a somewhat stronger β dependence than that observed with a thermal energy confinement scaling of $B\tau \propto \beta^{-0.7}$. More than half of the β scaling is found to result from finite β effects in model. The model demonstrates a collisionality scaling of $B\tau \propto \nu_*^{-0.3}$ with some unfavorable dependence arising from neoclassical transport in the plasma core region. The overall goodness-of-fit obtained when comparing the global and local predictions results in a root-mean-square error averaging less than 13% for the total stored energy and averaging less than 9% for the density and temperature profiles relative to the maximum experimental values. When $E \times B$ shear effects are added to the model, the resulting change in the mean RMS error for the temperature profiles is less than 4%.

I. INTRODUCTION

It has been widely demonstrated that the radial electron and ion thermal transport drop significantly after a low to high confinement (L-H) transition [1]. At the transition a transport barrier is formed, leading to rapid increases in the edge temperatures and to the formation of a steep pedestal region in the electron density profile. This high confinement mode or H-mode [2] was first observed in the ASDEX tokamak [3] and was one of the earliest achieved enhanced confinement regimes identified in tokamaks. However, there is no physical model that can accurately predict when the L-H transition occurs and how the boundary density and temperatures subsequently respond in time. Furthermore, it is unclear whether or not the core plasma region can be described by the same physics responsible for anomalous transport in L- and H-mode. Recently, the ITER Transport Modeling and Database Group [4] has assembled a standardized profile database including full experimental analyses of the density and temperature profiles as well as the various sources and sinks. Model testing using this database has focused on comparing various transport models with steady-state temperature profiles and computed standardized figures of merit [4,5]. While useful for assessing the performance of a given model, the temporal response is not addressed nor is the predicted particle transport (if at all present). Unlike transport analyses conducted with steady-state codes, predictive simulations self-consistently compute the sources as the profiles evolve in time. The goal of this work has been to develop a theoretically based transport model capable of accurately predicting both particle and thermal transport in Ohmic, L-mode and H-mode plasmas and ultimately allowing confident extrapolation to future machines. Recent work has focused on applying precisely the same Multi-mode transport model benchmarked against a variety of Ohmic and L-mode plasmas [6–11] to study H-mode confinement in DIII-D and JET plasmas. Results are presented here for 16 JET H-mode discharges taken from the ITER Profile Database that include pairs of dimensionally similar discharges comprising scans in normalized gyro-radius, collisionality, and β . By prescribing the boundary densities and temperatures according to analyses of the experi-

mental data, this transport model successfully predicts the electron density and temperature profiles during the H-mode phase without any alteration of the transport coefficients.

First, an overview of the transport model and methodology is provided. A description of the experimental data is then given in Section 2. Here, the data is summarized providing relevant discharge parameters and grouped according to matched pairs of discharges comprising scans in normalized gyro-radius, collisionality, plasma β , and density. Details of the results are summarized in Section 3. Section 4 provides statistical measures of the quality of fit to experimental data in terms of both local and global quantities. In Section 6, the results of including $E \times B$ shear are described. Concluding remarks are given in Section 7.

II. TRANSPORT MODELING

In this article, predictive simulations are carried out using the same version of the Multi-mode transport model previously described in Ref. [6,7,10,11] using the BALDUR 1-1/2 D transport code. This model combines the Weiland ion temperature gradient (ITG) and trapped electron mode (TEM) model [12–16] with the Guzdar-Drake resistive ballooning mode model [10,17,18] together with smaller contributions from kinetic ballooning modes and neoclassical transport to describe the radial particle and thermal transport in the plasma core. The ITG/TEM part of the model is the same model used in other simulations of JET discharges but generalized to include finite β effects and the effects of parallel ion motion [19]. For the H-mode plasmas studied here, both the edge collisionality and the average toroidal β values are low enough that the contributions to the total transport from the ballooning modes are small, thus simplifying analysis of the modeling results. In applying the Multi-mode model, the same simulation methodology described in Refs. [11,20] is followed with the boundary conditions applied at a normalized radius of $\hat{\rho} = 0.975$ which is close to the top of the density and temperature pedestal in these JET H-mode discharges. Here, $\hat{\rho} = \rho/\rho(a)$ with $\rho = [\Phi/(\pi B_T)]^{1/2}$, where Φ is the toroidal flux, B_T is the toroidal field and a is the minor radius. At this radius, experimentally analyzed data is used to prescribe the boundary densities and temperatures as a function of time. As discussed in the next section, a number of the JET discharges contained helium. This was accounted for in the simulations by programming the specified helium fraction at the boundary location and adjusting the influx rate to maintain a constant average helium fraction as a function of time. The volume averaged impurity content is determined by prescribing the impurity content at the edge of the plasma and by influxing 40 eV impurity neutral atoms as a function of time. All simulations were initiated in the Ohmic phase and follow the full time evolution of the predicted densities and temperatures up to the time of interest during the H-mode phase. The simulations are self-consistent in that the sources, sinks and equilibrium are computed using the model predicted profiles as they evolve in time.

III. EXPERIMENTAL DATA

Recently, the ITER Transport Modeling and Database Group [4] has assembled a standardized profile database which is readily available at the ITER U.S. Joint Central Team server. All data stored at this site is in the form of 1-D and 2-D text files. Considered in this study are sixteen JET ELMy H-mode discharges with diagnostic times chosen during a quasi-stationary phase. Included are three pairs of dimensionally similar ITER demonstration discharges where the normalized gyro-radius was varied by a factor of 1.6 while keeping all the other dimensionless variables held nearly fixed [21,22]. These discharges have various types, amplitudes, and frequency of ELMs and have an acceptable level of dimensionless similarity. Discharges 35156 and 35171, and 37944 and 37379, comprise matched pairs which were operating away from the H-mode power threshold and experimental analysis indicated that the confinement followed a gyro-Bohm scaling of $B\tau_{\text{th}} \propto \rho_*^{-2.7}$ in agreement with the ITER93-P scaling [23]. The other pair of discharges, 33131 and 33140, were, however, close to the power threshold and confinement was observed to be nearly Bohm-like [22]. With the exception of discharge 37944, which had a 2% ^3He content, these shots were fueled with deuterium. Discharges 38407 and 38415 are part of an ITER relevant β scan obtained using the new pump divertor [24]. In this scan, β was varied holding ρ_* , ν_* and other dimensionless quantities fixed. These plasmas contain 20 and 8% ^3He , respectively. The last set of dimensionless scaling experiments includes discharges 37728 and 37718 where ρ_* and β were held fixed as the collisionality varied by a factor of 2.6. The ^3He content in these pulses was 7 and 18%, respectively. Discharges 38287 and 38285 comprise a pair of discharges where the gas fueling was varied at fixed beam power [25]. The other four JET H-mode discharges considered include discharge 33465, which was part of a series of experiments designed to test gyro-radius scalings between various machines, discharge 32745, which was part of a divertor study [26] with 20% ^3He dilution, a high- ρ_* discharge, No. 35174 [22], and a high β discharge No. 34340.

With the exception of discharges 37728 and 33131, which also included 1.1 and 1.7 MW of absorbed ICRH, respectively, all are auxiliary heated with neutral beams only. The RF power was included in the TRANSP analyses of these discharges but contributed little to the total measured stored energy. In discharge 33131, the ICRH heating was a relatively smaller component in the total heating, thus affecting the stored energy even less than in discharge 37728.

Tables 1–4 summarize the experimental data at the chosen diagnostic time for each of the sixteen discharges. Table 1 groups the gyro-radius discharges, Table 2 describes the more recent gyro-radius and β experiments, Table 3 describes the collisionality and gas fueling experiments, and Table 4 includes the other four discharges. Provided are the major radius R_o and the minor radius a in metres, the average elongation κ and triangularity δ , the toroidal field B_T in teslas, the total plasma current I_p in megamps, the line-average density \bar{n}_e in units of $10^{19}m^{-3}$, the line averaged effective charge ($\bar{Z}_{\text{eff}} = \sum n_a Z_a^2 / n_e$), the experimental normalized Larmor radius at the plasma centre $\rho_*(0)$, the auxiliary heating power in megawatts, the thermal energy confinement time τ_{th} in seconds, the thermal and total stored energy W in megajoules, the sawtooth period τ_{saw} during the Ohmic and H-mode phases, the time of the last sawtooth crash prior to the diagnostic time t_{saw}^* , and the “diagnostic time” at which simulation results were compared with the experimental profiles. All the data provided in these tables was taken directly from the ITER Profile Database with the exception of discharge 38407, which has a confinement time based upon more detailed calculations [27].

TABLES

TABLE 1
Major plasma parameters for JET gyroradius experiments.

Tokamak	JET	JET	JET	JET
Shot	33131	33140	35156	35171
Type	Low ρ_*	High ρ_*	Low ρ_*	High ρ_*
R_o (m)	2.94	2.93	2.87	2.88
a (m)	0.94	0.92	0.93	0.94
κ_a	1.70	1.56	1.56	1.58
δ	0.28	0.26	0.11	0.24
B_T (T)	3.13	1.77	2.17	1.09
I_p (MA)	2.83	1.61	2.05	1.01
$\bar{n}_e(10^{19}\text{m}^{-3})$	7.10	3.65	5.44	2.44
\bar{Z}_{eff}	1.92	1.66	1.25	1.10
P_{NB} (MW)	18.0	5.80	8.60	2.91
τ_{th} (secs)	0.26	0.37	0.40	0.24
W_{th} (MJ)	7.14	2.09	2.90	0.82
W_{tot} (MJ)	7.85	0.96	3.08	0.96
τ_{saw}^{OH} (s)	0.15	0.15	0.15	0.15
τ_{saw}^H (s)	0.55	0.0	0.0	0.0
t_{saw}^* (s)	55.3	52.9	54.5	62.0
Diagnostic				
Time (s)	55.69	56.50	55.85	65.87

TABLE 2
Major plasma parameters for JET ρ_* and β experiments.

Tokamak	JET	JET	JET	JET
Shot	37944	37379	38407	38415
Type	Low ρ_*	High ρ_*	Low β	High β
R_o (m)	2.89	2.91	2.91	2.88
a (m)	0.92	0.92	0.94	0.97
κ_a	1.72	1.62	1.60	1.55
δ	0.37	0.19	0.16	0.11
B_T (T)	2.65	1.07	1.59	1.84
I_p (MA)	2.58	0.97	1.47	1.67
$\bar{n}_e(10^{19}\text{m}^{-3})$	5.95	1.71	3.05	4.02
\bar{Z}_{eff}	2.32	2.27	2.09	2.06
P_{NB} (MW)	11.6	3.70	5.60	15.7
τ_{th} (s)	0.43	0.21	0.31	0.20
W_{th} (MJ)	5.38	0.72	1.59	3.12
W_{tot} (MJ)	6.11	0.99	1.87	3.87
$\tau_{\text{saw}}^{\text{OH}}$ (s)	0.25	0.10	0.25	0.25
$\tau_{\text{saw}}^{\text{H}}$ (s)	0.71	0.26	0.31	0.48
t_{saw}^* (s)	59.9	63.2	57.2	56.4
Diagnostic				
Time (s)	60.14	63.39	57.40	56.61

TABLE 3
Major plasma parameters for JET ν_* and gas fueling experiments.

Tokamak	JET	JET	JET	JET
Shot	37728	37718	38287	38285
Type	Low ν_*	High ν_*	Low Gas	High Gas
R_o (m)	2.92	2.94	2.90	2.89
a (m)	0.96	0.93	0.93	0.94
κ_a	1.64	1.58	1.64	1.61
δ	0.20	0.13	0.20	0.19
B_T (T)	2.71	2.11	2.61	2.61
I_p (MA)	2.57	1.97	2.57	2.56
$\bar{n}_e(10^{19}\text{m}^{-3})$	4.90	4.54	5.72	6.57
\bar{Z}_{eff}	1.76	1.93	1.85	1.92
P_{NB} (MW)	13.3	9.70	11.3	11.5
τ_{th} (secs)	0.24	0.29	0.50	0.35
W_{th} (MJ)	4.24	2.75	5.32	3.74
W_{tot} (MJ)	4.89	3.09	5.82	4.03
$\tau_{\text{saw}}^{\text{OH}}$ (s)	0.25	0.25	0.25	0.25
$\tau_{\text{saw}}^{\text{H}}$ (s)	0.51	0.41	0.82	0.60
t_{saw}^* (s)	57.8	55.3	56.0	57.3
Diagnostic				
Time (s)	58.12	55.38	56.61	58.39

TABLE 4
Major plasma parameters for the miscellaneous JET discharges.

Tokamak Shot	JET 33465	JET 32745	JET 35174	JET 34340
Type	Identity	D-He	High ρ_*	High β
R_o (m)	2.87	2.87	2.87	2.87
a (m)	0.95	0.88	0.95	0.88
κ_a	1.55	1.69	1.56	1.66
δ	0.19	0.18	0.22	0.15
B_T (T)	1.10	2.96	1.10	2.16
I_p (MA)	1.04	3.04	1.02	2.03
$\bar{n}_e(10^{19}\text{m}^{-3})$	3.26	7.34	2.49	5.54
\bar{Z}_{eff}	1.52	1.64	1.48	1.99
P_{NB} (MW)	2.77	16.2	6.92	17.7
τ_{th} (secs)	0.37	0.54	0.17	0.24
W_{th} (MJ)	0.93	6.13	1.23	4.24
W_{tot} (MJ)	0.98	6.70	1.57	4.87
τ_{saw}^{OH} (s)	0.15	0.23	0.15	0.15
τ_{saw}^H (s)	0.0	0.47	0.47	0.54
t_{saw}^* (s)	63.0	56.0	62.74	55.28
Diagnostic Time (s)	63.76	56.44	64.38	56.37

IV. RESULTS OF SIMULATIONS

Using the same transport model without any alterations, it is found that the model is equally successful in predicting the density and temperature profiles for this set of JET H-mode discharges. In Fig. 1, the predicted total stored energy is plotted against the experimental values for 54 L-mode discharges from several machines along with the 16 JET H-mode discharges. For all 70 discharges the RMS error for the total stored energy is 11.6%. Here, the hollow points denote the L-mode discharges while the solid points denote the JET H-mode discharges. Overall, the level of agreement with the JET H-mode discharges is consistent with previous results for L-mode plasmas [7–9,11] using the BALDUR time dependent transport code. Taking the pedestal density and temperature values from experimental data at 97.5% of the minor radius, the simulations yield an improvement of H-mode confinement over L-mode and flatter density profiles as observed in the experiments. No significant particle pinch is predicted by the Weiland ITG model unlike that found in L-mode simulations resulting in relatively flatter density profiles. Examining the thermal diffusivities, the ITG mode is found to be held closer to marginality over a greater portion of the plasma in comparison with L-mode plasmas. In addition, the ITG/TEM mode is predicted to be the more dominant mode in the outer region of H-mode plasmas and is therefore more directly affected by the edge temperature. Figure 2 compares the predicted ion thermal diffusivity for a typical JET L- and H-mode plasma. The reader is instructed to focus on the relative mix between the various modes contributing to the overall transport and not on the relative magnitudes of the total diffusivities between these two discharges, as they differ in many respects (auxiliary heating, density, etc.). Here, it is evident that the ITG/TEM mode is dominant over most of the plasma in H-mode plasmas, while the model predicts an additional and relatively larger contribution from the resistive ballooning mode near the edge of L-mode plasmas.

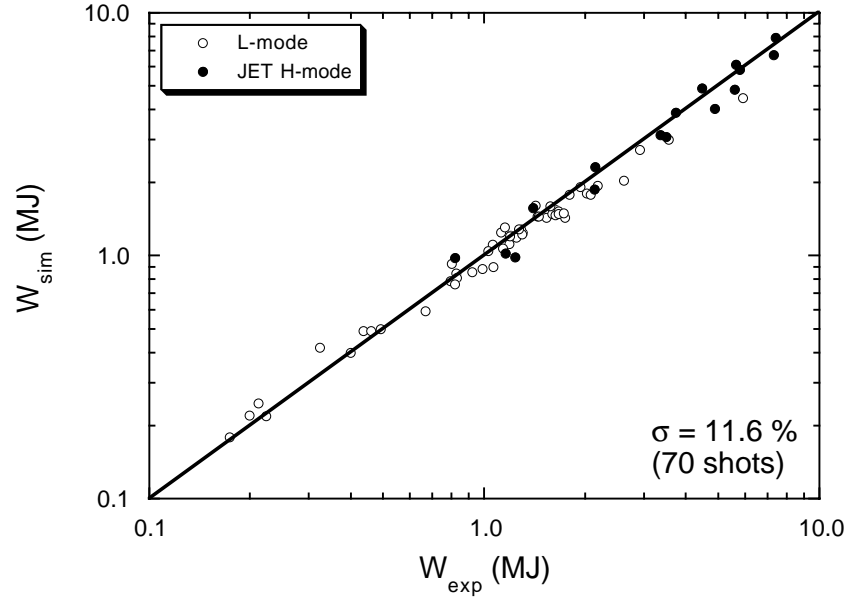


Fig. 1. Simulated versus experimental total stored energies for the 16 JET H-mode discharges studied here (solid circles) along with the the stored energies of 54 L-mode discharges from DIII-D, TFTR and JET (open circles). A perfect match to the experimental values is indicated with a solid diagonal line.

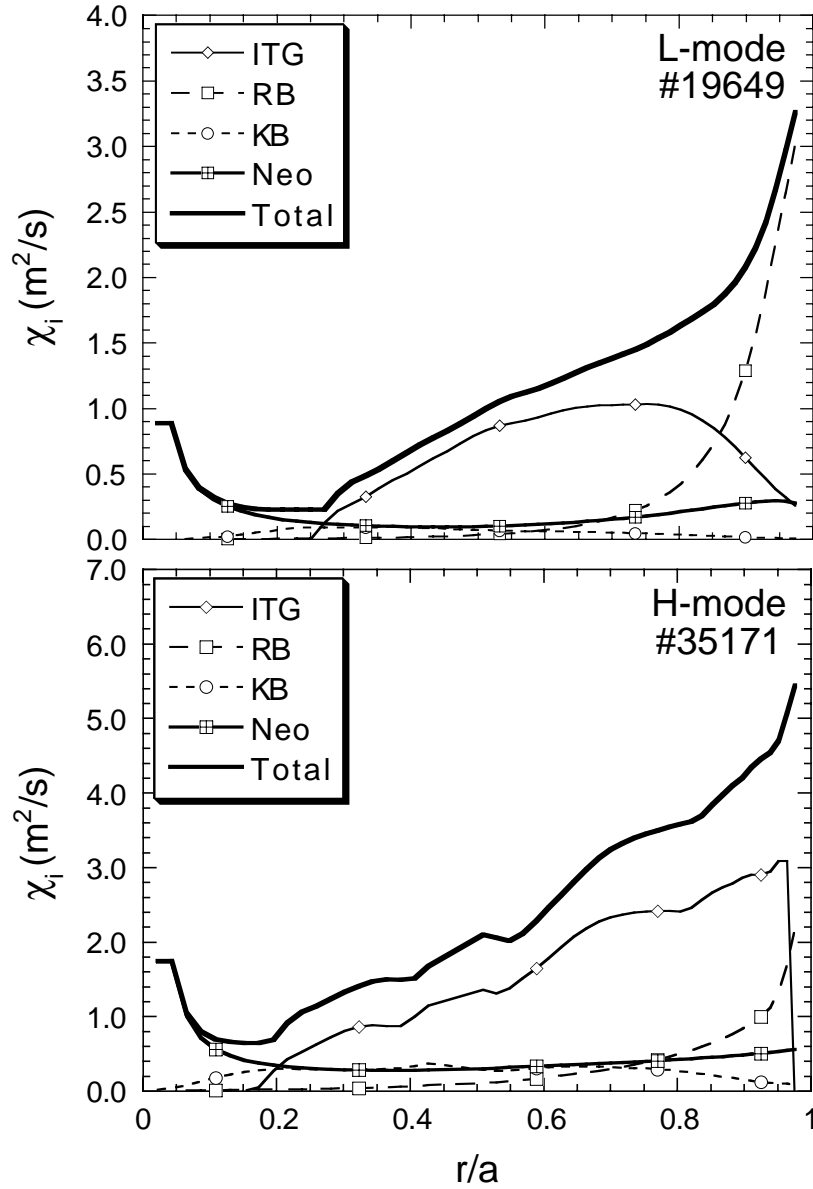


Fig. 2. Predicted ion thermal diffusivities for (a) a typical JET L-mode discharge and (b) a typical JET H-mode discharge. Shown are the individual mode contributions and total diffusivity (thick solid line). Here, ITG indicates drift waves; RB the resistive ballooning mode; KB the kinetic ballooning mode; and Neo the neoclassical transport.

A. Gyroradius Experiments

In a gyroradius scan, where all the other dimensionless parameters are held fixed, the thermal energy confinement is expected to scale with the toroidal field as

$$\tau_{\text{th}} \propto B_T^{(1+2x_\rho)/3} \quad (1)$$

assuming scale invariance such that the thermal diffusivity is assumed to depend only on local dimensionless variables [28,29]. Here, the scaling exponent would be $x_\rho = 1$ for gyroBohm scaling, $x_\rho = 0$ for Bohm scaling, $x_\rho = -1/2$ for Goldston scaling and $x_\rho = -1$ for stochastic scaling due to ergodic field lines. In analyzing the simulations of the three pairs of gyro-radius scans, small imperfections in dimensionless parameters (i.e. collisionality and beta) lead to an apparent confinement scaling that is stochastic scaling ($\tau \propto B_T^{0.8}$) in the first pair, midway between gyroBohm and Bohm in the second pair ($\tau \propto B_T^{1.7}$) and better than gyroBohm scaling ($\tau \propto B_T^3$) in the third pair. Figures 3 and 4 show profiles of electron density, electron temperature and ion temperature for the second pair of gyroradius discharges (Nos. 35171 and 35156, respectively) plotted against the normalized minor radius. The points indicate the experimental data and the solid lines denote the simulation. To keep the collisionality and β constant at fixed geometry as the normalized gyroradius is varied, the density must be scaled as $n_e \propto B^{4/3}$ and the temperature as $T \propto B^{2/3}$.

As shown in previous studies of L-mode gyroradius experiments, deviations away from perfect dimensionless similarity can cause a purely gyroBohm transport model to exhibit worse than gyroBohm confinement [7]. Specifically, it was found that systematic changes in the profiles lead to differences in the collisionality and pressure gradient between one end of the scan and the other that resulted in an apparent non-gyroBohm scaling of the predicted energy confinement time. For these H-mode discharges, the same behavior is evident in the simulations and manifests itself in several ways. Experimentally, the pedestal region is particularly difficult to control when ELM activity is present, thus making H-mode similarity experiments intrinsically prone to mismatches in the edge profiles. By enforcing the boundary conditions at 97.5% of the minor radius where a significant portion of the

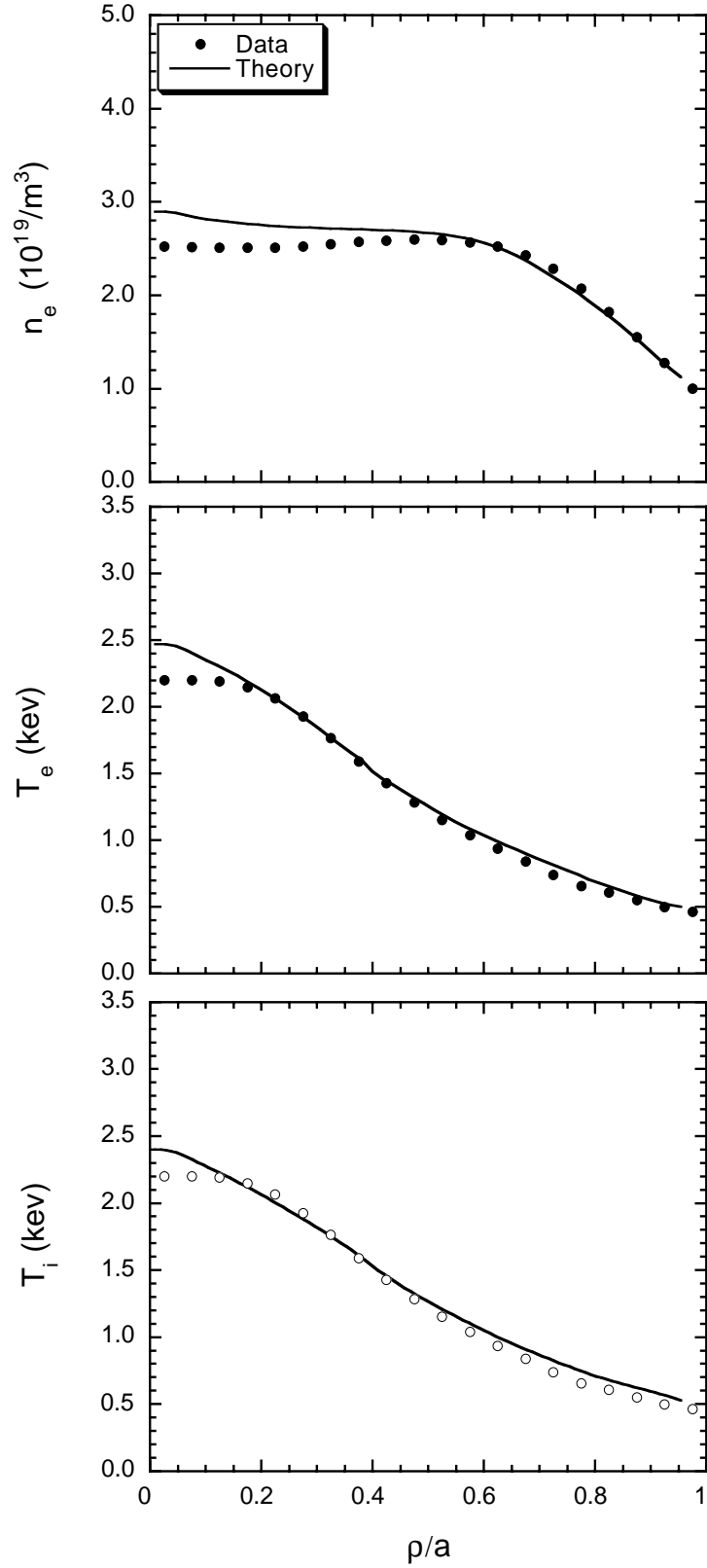


Fig. 3. Electron density and electron and ion temperature profiles for a high- ρ_* discharge, No. 35171, at 65.87 s. The solid circles and the open circles denote the data and the solid curves denote the simulation.

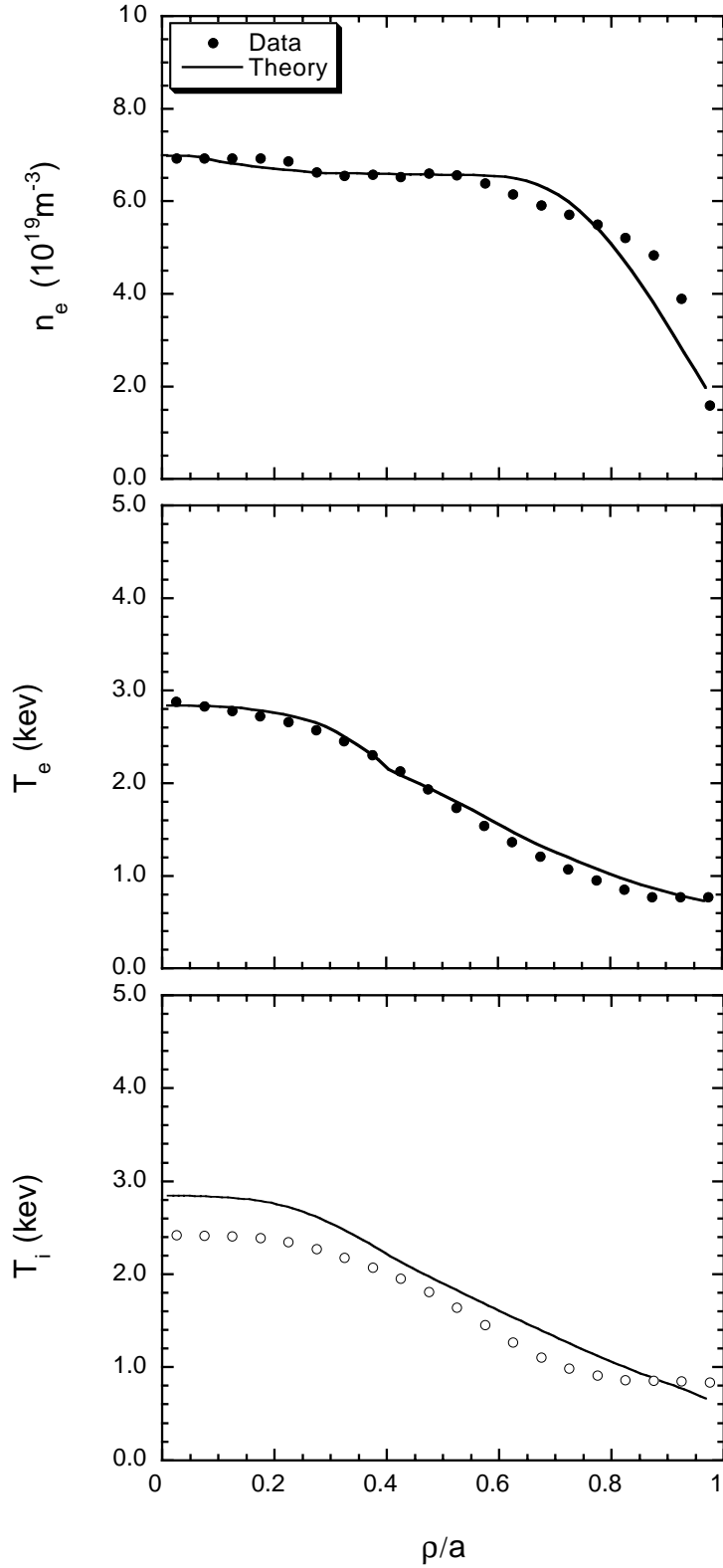


Fig. 4. Electron density and electron and ion temperature profiles for the low- ρ_* discharge, No. 35156, at 55.85 s. The solid circles and the open circles denote the data and the solid curves denote the simulation.

stored energy content lies, any imperfections in the profiles there can lead directly to non-trivial changes in global confinement. This was especially evident in the first pair of ρ_* discharges (Nos. 33140 and 33131), where both the experimental and the predicted energy confinement exhibited a nearly stochastic scaling. Inside $\hat{\rho} = 0.7$ the predicted scaling of the thermal diffusivities is gyroBohm-like, but mismatches in dimensionless parameters near the top of the pedestal (mainly q , ν_* and density gradient scale length L_n) result in an observed global confinement scaling that is significantly worse than gyroBohm. Unlike in L-mode conditions, the profiles are predicted to be closer to ITG marginality in the H-mode over much of the plasma core and are thus more sensitive to small deviations in the profiles. Overall, this is another illustration of how imperfections in dimensionally similar discharges can mask the underlying ρ_* dependence and cause a transport model to yield an apparent scaling that is significantly different from its intrinsic gyro-radius scaling while successfully reproducing the profiles within the uncertainty of the data.

B. β Scaling Experiments

Empirical scaling relations for H-mode energy confinement exhibit a strong unfavorable β scaling suggesting electromagnetic effects, such as magnetic flutter, are important. For example, the ITER-93P H-mode confinement scaling [23] gives $\tau_E \propto \beta^{-1.2}$. On the other hand, theories based upon $E \times B$ transport predict no degradation in confinement or even some level of stabilization in thermal transport with increasing β [30]. Thus, experimentalists and theoreticians have been strongly motivated to create and study experiments specifically designed to discern the exact nature of the β dependence in anomalous heat transport [24,31–33]. To vary β while keeping ρ_* , ν_* and q constant at fixed geometry, the plasma parameters are scaled as $n \propto B^4$, $T \propto B^2$ and $I \propto B$. In 1996, it was first reported that an energy confinement scaling of $B\tau \propto \beta^{-0.1}$ was observed in JET, in agreement with the DIII-D experimental findings [32,33]. Examination of the data supplied to the ITER Profile Database for these discharges indicates imperfections in dimensionless similarity. To keep ρ_* and ν_* fixed, the density should have been scaled by a factor of 1.8 ($n \propto B^4$) going from low to high β . However, the electron density varied by only a factor of 1.3 (see Table 2). Therefore, interpretation of this data is sensitive to the model assumptions made. Assuming that the stored energy scales as $W \propto nT \propto B^6 a^5$, β can be taken to scale as

$\beta_{\text{th}} \propto W_{\text{th}} B^{-2}$. Taking the values for the thermal stored energy W_{th} , energy confinement time τ_{th} and toroidal field B_T from Table 2, a confinement scaling of $B\tau_{\text{th}} \propto \beta_{\text{th}}^{-0.8}$ is found for a 1.47 factor scan in β . However, this scaling does not include any corrections due to mismatches in, for example, ρ_* and ν_* . A comparison of the local dimensionless variables indicates that ν_* varied by approximately 1.5 and that ρ_* varied by as much as 8%. Assuming a collisionality scaling of $B\tau \propto \nu_*^{-0.27}$ as derived from the JET ν_* experiments [32], this gives a $B\tau$ correction factor of 1.1. Taking a gyroBohm transport scaling of $B\tau \propto \rho_*^{-3}$ gives an additional correction factor of 0.8. Combining these corrections then yields an effective scaling of $B\tau_{\text{th}} \propto \beta_{\text{th}}^{-0.4}$. This scaling result, coincidentally, agrees with the result obtained by simply taking $B\tau \propto B^{-4\alpha} a^{5\alpha}$, which assumes that ρ_* and ν_* are perfectly matched. In any case, using different modeling assumptions or diagnostic times different from those given in Table 2 could yield different scaling results [27].

Examination of the simulations indicates that good agreement with the time evolution of the density and temperature profiles is obtained for both discharges in the β scan. Figure 5 shows the time evolution of a high- β discharge, No. 38415, beginning in the Ohmic phase at 53.0 s and going into the sawtoothed H-mode phase until the time of interest at 56.61 s. An L-H transition promptly follows the application of neutral beam power at 54.0 s. The predicted and experimental central electron and ion temperatures along with the total stored energy are shown. Examining the match in dimensionless parameters of the simulations, it is found that the largest mismatch occurs in ρ_* at the diagnostic times listed in Table 2. There is also a 20% difference in ν_* near $\hat{\rho} = 0.9$ and as much as a 10% difference in T_i/T_e inside $\hat{\rho} = 0.5$. The predicted $B\tau$ values yield a slight β degradation, with a scaling of $\beta^{-.7}$. The source of this degradation results partly from mismatches in dimensionless parameters near the top of the pedestal and partly from finite- β effects in the model.

In the Weiland drift wave model, finite β effects are included but were derived for circular geometry [15]. This tends to result in a lower critical electron β for the ideal ballooning mode threshold. As evident in the simulation of the high- β discharge, the ideal threshold is exceeded in the inner 25% of the plasma radius resulting in higher thermal diffusivities from the ITG mode. At low β the finite- β effects stabilize the ITG mode while at high β they destabilize it. In turning off the finite- β effects in the model, the resulting RMS error in the temperature profiles changed by less than 1% while the central β increased by 0.5%. While

producing only small changes in the profiles, finite β effects are responsible for half of the predicted β scaling. Without finite β effects included, a confinement scaling of $B\tau_{\text{th}} \propto \beta_{\text{th}}^{-0.4}$ is predicted in agreement with the experimental data.

Examination of growth rates across the plasma indicates that both the ITG mode and TEM mode are predicted to be unstable. Selecting parameters at a minor radius of 60.5 cm and varying the normalized temperature gradient g_t (electrons and ions together) around the simulation point, it is found that the relative stiffness (temperature gradient dependence) differs between the electron channel and the ion channel. As seen in Fig. 6, the slope of the effective ion thermal diffusivity is much steeper than that of the electron channel. Here, the diffusivities are shown plotted against the normalized hydrogenic ion temperature gradient $g_{\text{th}} = -R(dT_H/dr)/T_H$ with the simulation point at a normalized gradient of $g_{\text{th}} = 6.8$. While the growth rates exhibit the same slope for each channel, the ion channel has a stronger dependence of the heat flux on the normalized temperature gradient. This suggests that the ion channel may be more sensitive to variations away from perfect dimensionless similarity, resulting in an apparent difference in the scaling between the channels of transport when conducting a two fluid analysis of the data.

C. Collisionality Scaling Experiments

The other group of dimensionless similarity experiments constitutes a scan in collisionality ν while holding ρ_* , β and all the other dimensionless quantities fixed. This was done by scaling the density, temperature and current as $n \propto B^0$, $T \propto B^2$, and $I \propto B$, while holding the geometry fixed. In close agreement with the ITER-89P [34] and ITER-93P [23] confinement scalings, experimental analysis of these discharges indicated that $B\tau_{\text{th}}$ scaled as $\nu_*^{-0.27}$ [32]. This is consistent with the thermal transport scaling predicted for collisionless drift waves that are expected to be independent of collisionality [35]. The residual unfavorable scaling may be resulting from neoclassical transport, which has an unfavorable collisionality dependence in the banana regime. In the simulations, it is found that the neoclassical transport tends to dominate the total thermal transport near the magnetic axis. This is especially true for the ion channel. Examining the thermal diffusivities, it is found that the ITG mode is predicted to be stable inside $\hat{\rho} = 0.45$. Examination of the dimensionless parameters indicates that they are well matched with the exception of ρ_* . Correcting for

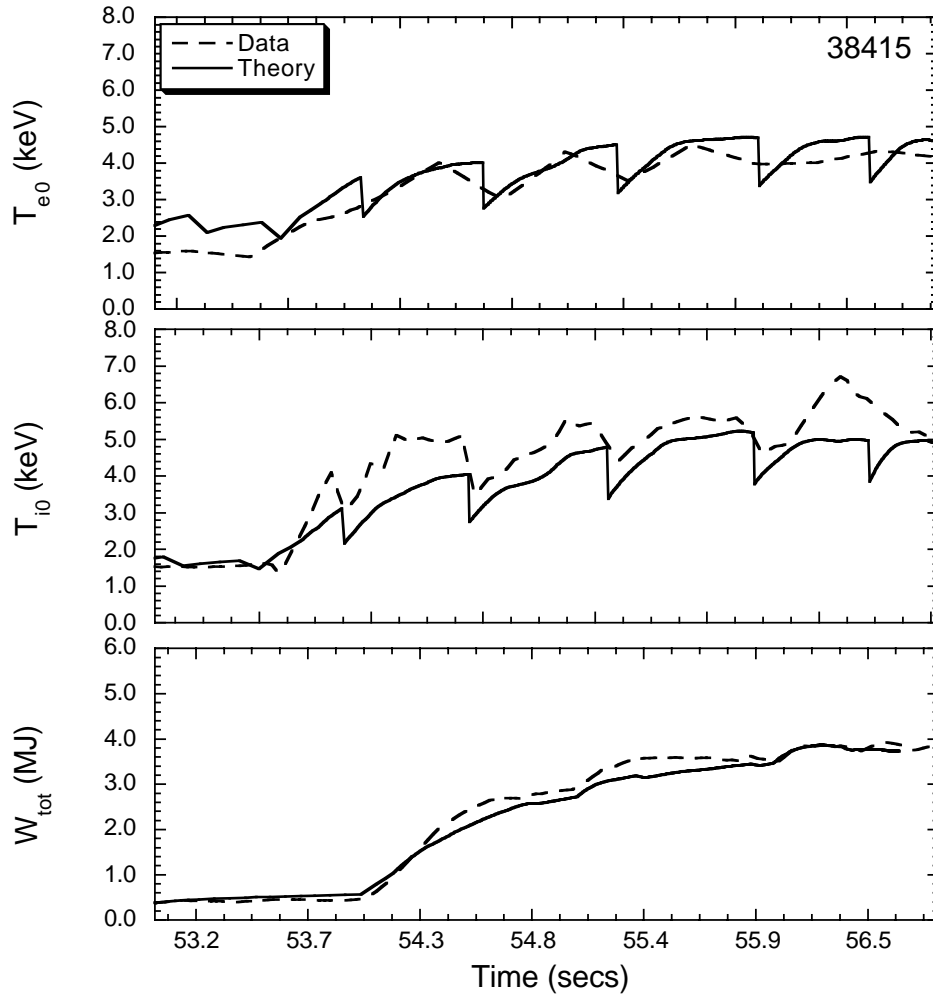


Fig. 5. Time evolution of the central temperatures and total stored energy content from the simulation (solid curve) and experiment (dashed curve) for the a high- β discharge, No. 38415.

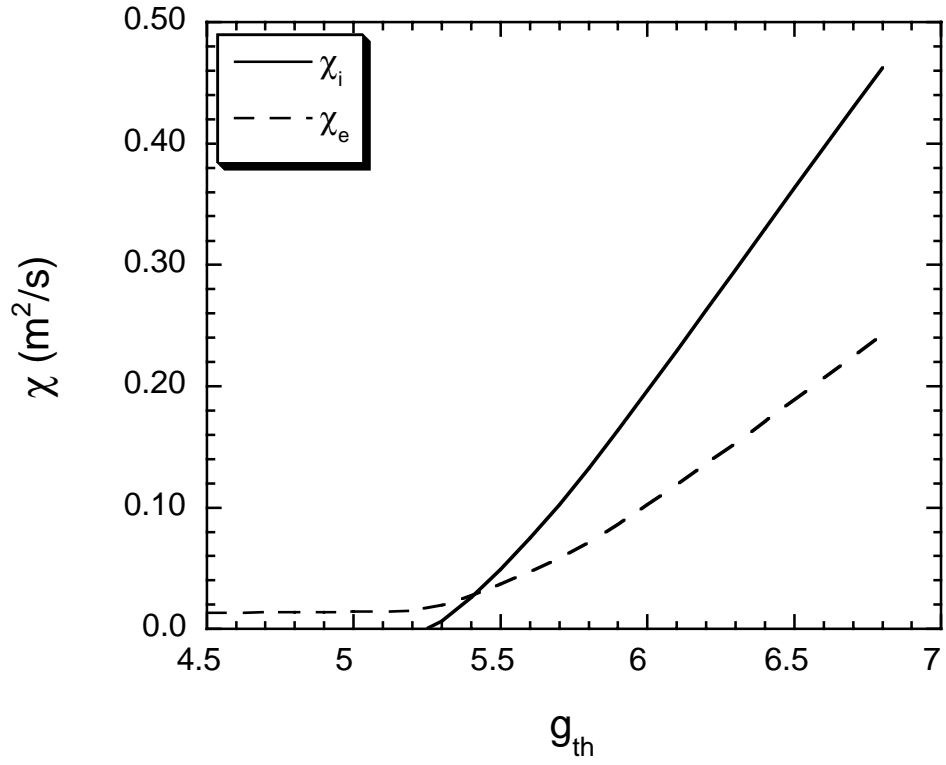


Fig. 6. Effective ion and electron diffusivities versus normalized ion temperature gradient $g_{th} = -R (d T_H/d r)/T_H$ for a high- β discharge, No. 38415, at a minor radius of 60.5 cm.

the slight mismatch in ρ_* assuming gyroBohm scaling, yields a predicted energy confinement scaling of $B\tau_{\text{th}} \propto \nu_*^{-0.3}$. However, the simulations indicate that the variation in ν_* between the discharges is not spatially constant. Near $\hat{\rho} = 0.5$, ν_* varied little, but $\hat{\rho} = 0.8$ it varied by approximately a factor of 2.6. This is also evident in the experimental profiles. Therefore, it is difficult to extract any global scaling on ν_* . Local analysis of the simulations indicates a collisionality scaling in the thermal diffusivities of $\chi \propto \nu_*^{0.0 \pm 0.25}$ in the region where the ITG and TEM modes are predicted to be unstable. In the inner core region where neoclassical transport becomes dominant, the observed collisionality scaling exponent α_ν rises to values consistent with an unfavorable linear dependence on collisionality, as described by neoclassical theory.

D. Gas Fueling Experiments

It has been previously reported that increasing the gas fueling rate can degrade the energy confinement in JET [22,25]. This appears to contradict the ITER-93P scaling [23], which exhibits a weak scaling with density of $\tau \sim n_e^{0.2}$. It has been suggested that the source of the degradation is associated with an increase in the ELM frequency (and subsequent losses) due to an increase in the pressure gradient in the pedestal region. In the simulations of the low (No. 38287) and high (No. 38285) gas fueling discharges, the reduction in confinement with density follows directly from a 40% decrease in the pedestal temperatures as the line averaged electron density increases from $5.7 \times 10^{19} m^{-3}$ to $6.6 \times 10^{19} m^{-3}$. The pedestal density remains nearly the same in the two discharges, and the increase in the line averaged density results from a peaking of the density inside $\hat{\rho} = 0.5$.

V. STATISTICAL MEASURES OF GOODNESS OF FIT

To quantify the goodness of fit, comparisons are made between the model predictions and the experimental data for the total stored energy and the profiles. Spanning a range from 1 MJ to nearly 8 MJ it is found that the model predictions for this set of JET H-mode discharges yields an RMS deviation of approximately 13%. Figure 7 shows the total stored energy offset f_W , defined as $W_s/W_x - 1$, for each discharge. Here, W_s and W_x denote the simulated and experimental stored energy values, respectively. In the lower left hand corner of Fig. 7, the average $\langle R_W \rangle$ and RMS error ΔR_W are also given where

$$\langle R_W \rangle = \sum_i (W_{si}/W_{xi}) / N \quad (2)$$

and

$$\Delta R_W = \sqrt{\sum_i (W_{si}/W_{xi} - 1)^2 / N} \quad (3)$$

with N as the total number of discharges. The local figures of merit include the offset f and RMS error σ for the density and temperature profiles. They are computed relative to the maximum experimental values and are defined as

$$f^{\text{rel}} = \frac{1}{N} \sum_{j=1}^N \epsilon_j / X_{\text{max}}^{\text{exp}} \quad (\%) \quad (4)$$

and

$$\sigma^{\text{rel}} = \sqrt{\frac{1}{N} \sum_{j=1}^N \epsilon_j^2} / X_{\text{max}}^{\text{exp}} \quad (\%) \quad (5)$$

where N is the total number of experimental data points and ϵ_j is the deviation between the j th experimental point X_j^{exp} and the corresponding simulation point X_j^{sim} such that $\epsilon_j = X_j^{\text{exp}} - X_j^{\text{sim}}$. The RMS error quantifies the scatter of the simulated profile about the experimental data while the offset determines the amount by which the overall simulated profile needs to be shifted upward or downward in order to minimize the RMS error.

Figure 8 shows the relative RMS error for the density and temperature profiles plotted for each discharge numbered. The maximum experimental values are provided in Table 5. The density errors are diagonally shaded while the electron and ion temperature error are denoted with solid and dotted shading, respectively. Here, the density profiles agree to within 9.2%, the electron temperature profiles to within 16% and the ion temperature profiles to within 21%. The largest RMS error appears for the high- β shot 34340, where the simulated ion temperature profile underpredicts the experimental profile ($f^{\text{rel}} = 15\%$).

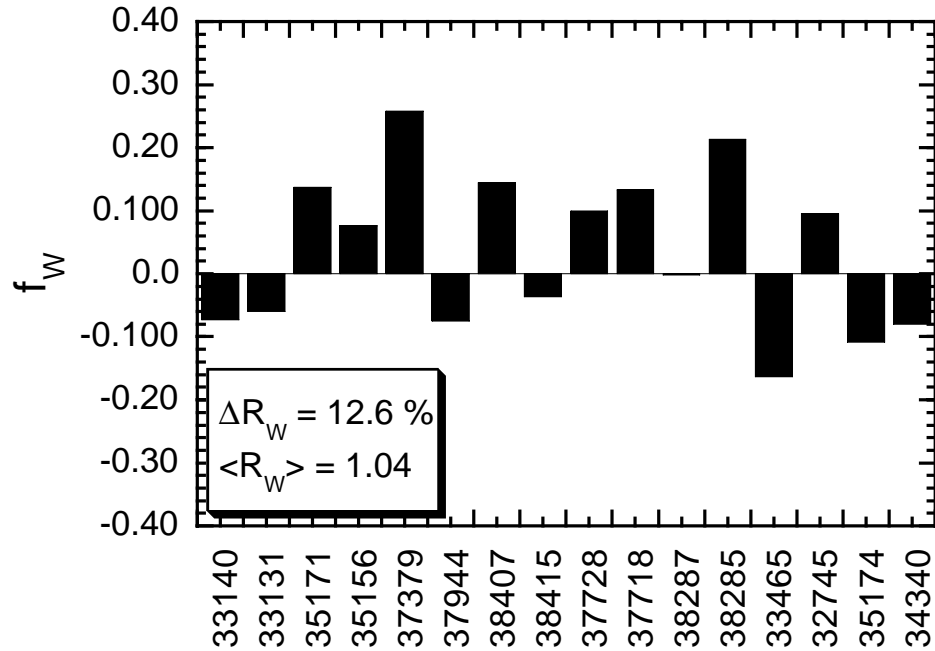


Fig. 7. Stored energy offset $f_W = W_s/W_x - 1$ versus discharge where W_s and W_x denote the simulated and experimental stored energy values, respectively. Also shown is the average error $\langle R_W \rangle$ and RMS error ΔR_W .

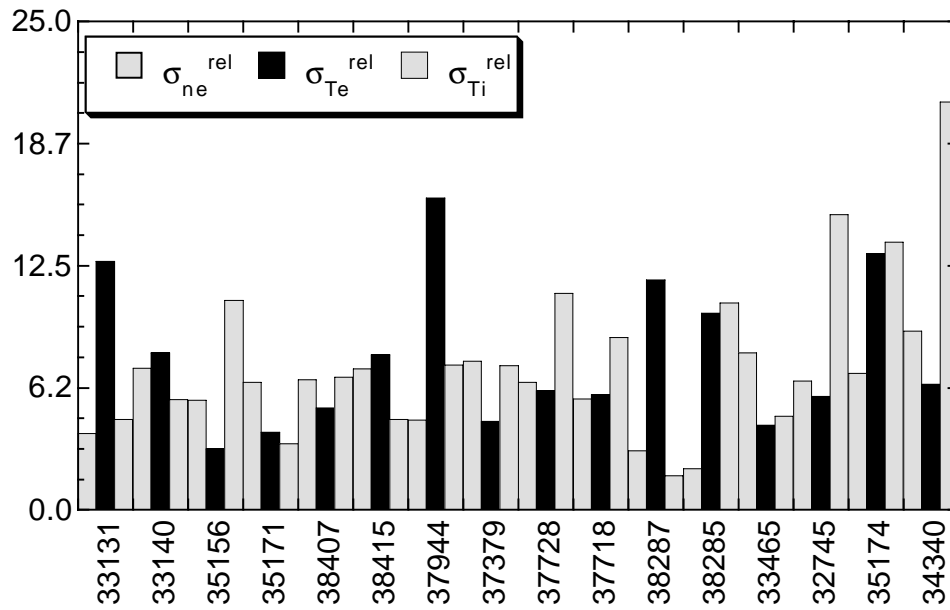


Fig. 8. Relative RMS error σ^{rel} (%) versus discharge for electron density and electron and ion temperature profiles.

TABLE 5
Maximum experimental densities and temperatures.

Shot	$n_{e,max}^{\text{exp}}$ (10^{19}m^{-3})	$T_{e,max}^{\text{exp}}$ (keV)	$T_{i,max}^{\text{exp}}$ (keV)
33131	8.48	6.35	5.60
33140	4.29	3.66	3.66
35156	6.94	2.94	2.45
35171	2.60	2.20	2.20
37944	6.42	4.84	4.65
37379	1.90	2.73	3.01
38407	3.54	3.72	3.91
38415	4.62	4.22	5.56
37728	5.67	6.25	6.03
37718	5.30	3.45	3.88
38287	6.44	4.24	5.30
38285	7.52	3.20	3.66
33465	3.76	1.58	1.58
32745	8.72	5.60	5.24
35174	2.90	3.33	3.31
34340	6.42	4.30	6.44

VI. $E \times B$ SHEAR STABILIZATION

All the simulations previously described in this article were conducted using the Multi-mode model without taking into account the effects of $E \times B$ rotational shear stabilization. However, recent theoretical work and experimental observations suggest that enhanced $E \times B$ shear is correlated with a reduction in transport. To assess the relative importance of $E \times B$ shear for the JET discharges studied here, it was included in the Weiland drift wave part of the model [36] following the same prescription given in Ref. [30]. Here, it is assumed that the net linear growth rate from the Weiland model is given as $\gamma_{\text{net}} = \gamma - \gamma_E - \gamma_*$, where γ is the eigenvalue growth rate in the absence of $E \times B$ shear, γ_E ($\approx (r/q)d(qv_{E \times B}/r)/dr$) is the $E \times B$ rotational shear rate and γ_* is the diamagnetic rotational shear rate. Once incorporated into the model, it was then applied to the same JET discharges using the MLT shooting code whereby the predicted temperature profiles were computed at the designated time-slices listed in Tables 1–4. Unlike the BALDUR time dependent transport code, the MLT code uses precomputed sources, sinks, equilibrium and density profiles from a power balance analysis as an input and predicts the temperature profiles. A solution for a model is found when the predicted power flows match the experimental power flows. While this approach is not self-consistent, it has the advantage of generating quick results. A detailed description of the MLT code is given in Ref. [37].

Using the experimental boundary conditions at $\hat{\rho} = 0.9$ and taking the sources, sinks, geometry, density profile and toroidal velocity from experiment, the temperature profiles were predicted using the Multi-mode model with and without the effects of $E \times B$ shear. Table 6 gives the RMS errors for five similarity pairs of JET discharges. Comparing the statistics with and without $E \times B$ shear it is difficult to identify any systematic trend. While some predictions benefited from including $E \times B$ shear effects, others did not. Figure 9 shows the predicted temperature profiles for the low and high- β cases with and without $E \times B$ shear effects.

TABLE 6
RMS errors on the temperature profiles with and without $E \times B$ shear.

Shot	no $E \times B$		$E \times B$	
	σ_{Te}	σ_{Ti}	σ_{Te}	σ_{Ti}
33131	0.10	0.09	0.06	0.21
33140	0.11	0.06	0.06	0.02
35156	0.04	0.09	0.06	0.14
35171	0.07	0.08	0.06	0.07
37944	0.09	0.07	0.11	0.09
37379	0.06	0.04	0.04	0.13
38407	0.09	0.02	0.04	0.09
38415	0.15	0.05	0.10	0.09
37728				
37718	0.12	0.03	0.06	0.12

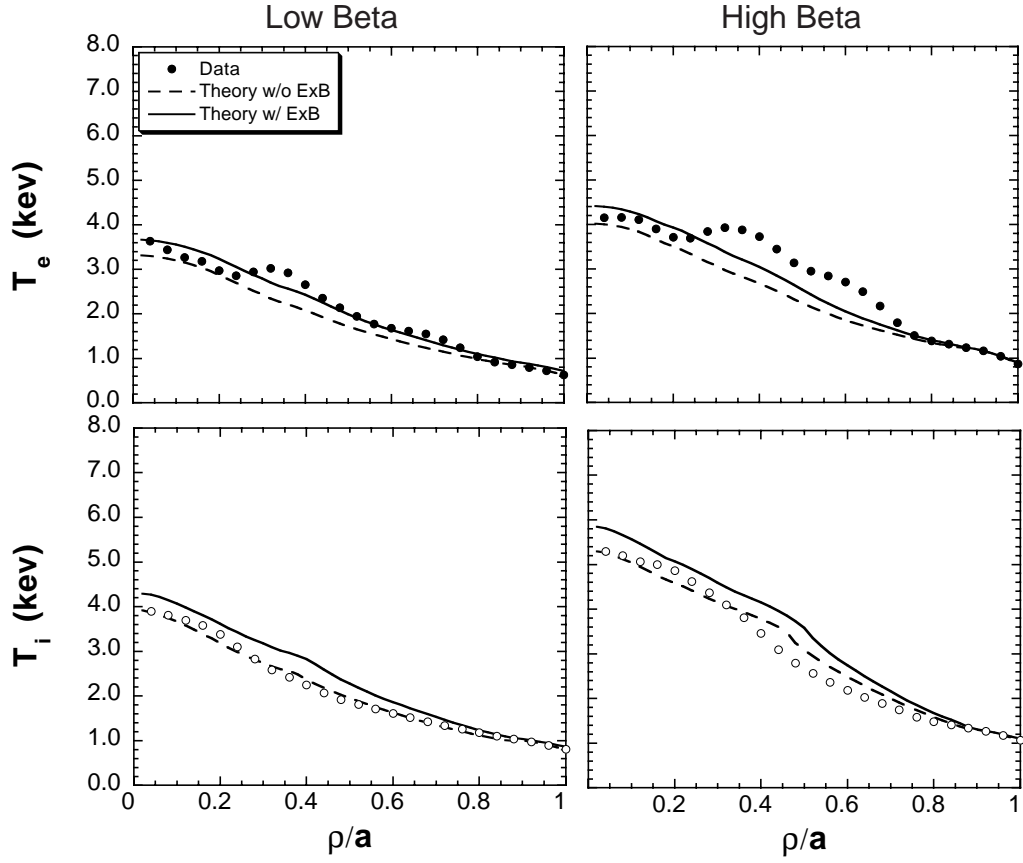


Fig. 9. Electron and ion temperature profiles for the low- and high- β discharges. The solid circles denote the data, the dashed curves denote the simulation without $E \times B$ shear and the solid curves denote the simulation with $E \times B$ shear.

VII. CONCLUSIONS

Time dependent simulations have been conducted for 16 JET ELMy H-mode plasmas including dimensionless parameter scans in the normalized gyroradius ρ_* , β , and collisionality ν_* . Using precisely the same theory based transport model applied to a wide variety of L-mode discharges, the average RMS error on the total stored energy is found to be 13%. The average RMS error for the profiles is 6.2% for the electron density, 7.8% for the electron temperature and 8.7% for the ion temperature. Taking the boundary conditions at the 97.5% radius, the improved confinement of the H-mode is predicted as are flatter density profiles in agreement with the experimental data. No alteration of the transport model is required. In general, these H-mode profiles remain closer to marginality than those in L-mode, and the predicted transport by the ITG mode becomes more sensitive to changes in the profiles.

As seen in previous simulations of L-mode gyroradius experiments, small deviations in dimensionless similarity can cause an intrinsically gyroBohm transport model to yield an apparent ρ_* confinement scaling that is worse than gyroBohm. It is also found that finite β effects in the model and mismatches in dimensionless parameters near the top of the pedestal result in an energy confinement scaling of $B\tau_{\text{th}} \propto \beta_{\text{th}}^{-0.7}$. Without finite- β effects included in the model, the predicted β scaling reduces to $B\tau_{\text{th}} \propto \beta_{\text{th}}^{-0.4}$ in closer agreement with the experimental results. Further analysis of the β scan simulations indicates that the presence of both the TEM mode and the ITG mode can lead to differing levels of stiffness (temperature gradient dependence) between the electron and ion channels. Therefore, small imperfections in dimensionless similarity can affect differently the scaling of the local transport of the electrons and ions. In simulations of the collisionality scan, it is found that the ITG mode is unstable closer to the magnetic axis as ν_* decreases resulting in a change in the relative mix between neoclassical and anomalous thermal transport as ν_* is varied. A global collisionality scaling of $B\tau_{\text{th}} \propto \nu_*^{-0.3}$ is predicted. Here, it is found that the unfavorable collisionality dependence results from the neoclassical transport contributing more to the overall thermal transport in the low- ν_* case. While the model exhibits a weak scaling with density, the

predicted confinement time was found to degrade significantly with the density in simulations of the gas fueling scan. Here, the reduction in confinement with density follows directly from a 40% decrease in the pedestal temperatures as the line averaged electron density increased by 15%.

The effects of $E \times B$ shear have been added to the model. While agreement with the experimental temperature profiles is improved for some cases, it is not for others. It is found that for this set of JET H-mode discharges, $E \times B$ shear stabilization is predicted to be relatively small with the change in the mean RMS error for the temperature profiles being less than 4%. No systematic trend was evident, but within the pairs of similarity discharges the amount of $E \times B$ shear stabilization did vary, thus affecting the observed scaling of the model.

REFERENCES

- [1] Groebner, R. J., Phys. Fluids B **5** (1993) 2343.
- [2] The ASDEX Team, Nucl. Fusion **29** (1989) 1959.
- [3] Wagner, F., et al., Phys. Rev. Lett. **49** (1982) 1408.
- [4] Connor, J. W., et al., in Fusion Energy 1996 (Proc. of the 16th Int. Conf. Montréal, 1996) Vol. 2, IAEA, Vienna (1997) 935.
- [5] Mikkelsen, D. R., ITER Confinement Database and Modeling Working Group, “Tests of 1-d transport models and their predictions for ITER”, F1-CN-69/ITERP1/08, paper presented at 17th IAEA Conf. on Fusion Energy, Yokohama, 1998.
- [6] Bateman, G., Kritz, A. H., Kinsey, J. E., Redd, A. J., and Weiland, J., Phys. Plasmas **5** (1998) 1793.
- [7] Kinsey, J. E. and Bateman, G., Phys. Plasmas **3** (1996) 3344.
- [8] Kinsey, J. E., Bateman, G., Kritz, A. H., and Redd, A., Phys. Plasmas **3** (1996) 561.
- [9] Bateman, G., Kinsey, J. E., Kritz, A. H., Redd, A. J., and Weiland, J., in Fusion Energy 1996 (Proc. of the 16th Int. Conf. Montréal, 1996) Vol. 2, IAEA, Vienna (1997) 559.
- [10] Kinsey, J. E. and Bateman, G., Phys. Plasmas **4** (1997) 2307.
- [11] Redd, A. J., Kritz A. H., Bateman, G., and Kinsey, J. E., Phys. Plasmas **4** (1997) 2207.
- [12] Bateman, G., Weiland, J., Nordman, H., Kinsey, J. E., and Singer, C., Phys. Scr. **51** (1995) 597.
- [13] Nordman, H., Weiland, J., and Jarmén, A., Nucl. Fusion **30** (1990) 983.
- [14] Fröjdth, M., Liljeström, M., and Nordman, H., Nucl. Fusion **32** (1992) 419.
- [15] Weiland, J. and Hirose, A., Nucl. Fusion **32** (1992) 151.
- [16] Jarmén, A. and Fröjdth, M., Phys. Fluids B **5** (1993) 4015.
- [17] Guzdar, P. N., Drake, J. F., McCarthy, D., and Hassam, A. B., Phys. Fluids B **5** (1993) 3712.

- [18] Drake, J. F., Univ. of Maryland, Annapolis, personal communication, 1995.
- [19] Strand, P., Nordman, H., Weiland, J., Christiansen, J. P., Nucl. Fusion **38** (1998) 545.
- [20] Kinsey, J. E., Singer, C., Cox, D., and Bateman, G., Phys. Plasmas **2** (1995) 811.
- [21] Balet, B., et al., in Controlled Fusion and Plasma Physics (Proc. 22nd Eur. Conf. Bournemouth, 1995), Vol. 19C, Part I, European Physical Society, Geneva (1995) 9.
- [22] Cordey, J. G., et al., Plasma Phys. Controlled Fusion **38** (1996) 67.
- [23] ITER Confinement Database and Modeling Group (presented by S. M. Kaye), in Plasma Physics and Controlled Nuclear Fusion Research 1994 (Proc. 15th Int. Conf. Seville, 1994), Vol. 2, IAEA, Vienna (1995) 525.
- [24] Christiansen, J. P., et al., in Controlled Fusion and Plasma Physics (Proc. 24th Eur. Conf. Berchtesgaden, 1997), Vol. 21A, Part I, European Physical Society, Geneva (1997) 89.
- [25] Matthews, G. F., et al., *ibid.*, Part III, p. 1045.
- [26] Campbell, D. J., et al., Plasma Phys. Controlled Fusion **38** (1996) 1497.
- [27] Stubberfield, P. M. and Cordey, G., JET Joint Undertaking personal communication, 1998.
- [28] Kadomstev, B. B., Sov. J. Plasma Phys. **1** (1975) 295.
- [29] Connor, J. W. and Taylor, J. B., Nucl. Fusion **17** (1977) 1047.
- [30] Waltz, et al., Phys. Plasmas **4** (1997) 2482.
- [31] Scott, S. D., et al., in Plasma Physics and Controlled Nuclear Fusion Research 1992 (Proc. 14th Int. Conf. Würzburg, 1994), Vol. 3, IAEA, Vienna (1993) 427.
- [32] Cordey, J. G., JET Team, in Fusion Energy 1996 (Proc. of the 16th Int. Conf. Montréal, 1996) Vol. 2, IAEA, Vienna (1997) 603.
- [33] Petty, C. C., et al., Nucl. Fusion **38** (1998) 1183.
- [34] Yushmanov, P. N., et al., Nucl. Fusion **30** (1990) 1999.

- [35] Connor, J. W., Plasma Phys. Controlled Fusion **30** (1988) 619.
- [36] Bateman, G., et al., Improving the theoretical foundations of the Multi-mode transport model, F1-CN-69/THP2-19 paper presented at 17th IAEA Conf. on Fusion Energy, Yokohama, 1998.
- [37] Konings, J. A. and Waltz, R. E., Nucl. Fusion **37** (1997) 863.

ACKNOWLEDGEMENTS

This work was supported by the United States Department of Energy, under Contract No. DE-FG03-95ER54309.

The author would like to thank A. Kritz and G. Bateman at Lehigh University for their support of this work. I would also like to extend my gratitude to P. Stubberfield, B. Balet, J. Christiansen and the JET Team for providing the experimental data and D. Boucher for processing and storing the data on the ITER Profile Database server at the ITER Joint Central Team work site in San Diego.